ADVANCED FUNCTIONAL MATERIALS
www.afm-journal.de

Room-Temperature Solid-State Nitrogen-Based Magneto-Ionics in $Co_xMn_{1-x}N$ Films

Nicolau López-Pintó, Christopher J. Jensen, Zhijie Chen, Zhengwei Tan, Zheng Ma, Maciej Oskar Liedke, Maik Butterling, Andreas Wagner, Javier Herrero-Martín, Enric Menéndez, Josep Nogués, Kai Liu, and Jordi Sort**

The increasing energy demand in information technologies requires novel low-power procedures to store and process data. Magnetic materials, central to these technologies, are usually controlled through magnetic fields or spin-polarized currents that are prone to the Joule heating effect. Magneto-ionics is a unique energy-efficient strategy to control magnetism that can induce large non-volatile modulation of magnetization, coercivity and other properties through voltage-driven ionic motion. Recent studies have shown promising magneto-ionic effects using nitrogen ions. However, either liquid electrolytes or prior annealing procedures are necessary to induce the desired N-ion motion. In this work, magneto-ionic effects are voltage-triggered at room temperature in solid state systems of $Co_xMn_{1-x}N$ films, without the need of thermal annealing. Upon gating, a rearrangement of nitrogen ions in the layers is observed, leading to changes in the co-existing ferromagnetic and antiferromagnetic phases, which result in substantial increase of magnetization at room temperature and modulation of the exchange bias effect at low temperatures. A detailed correlation between the structural and magnetic evolution of the system upon voltage actuation is provided. The obtained results offer promising new avenues for the utilization of nitride compounds in energy-efficient spintronic and other memory devices.

1. Introduction

The rapid growth of nanoelectronics and the advent of artificial intelligence are creating a huge demand for new materials and device architectures to store and process exponentially growing amounts of data in a faster, more energy-efficient and versatile manner.[1] With magnetism being at the heart of big data centers and hard disk drives in personal computers, magnetization switching between two states is a requirement for magnetic memory and spintronic devices. This is typically achieved through magnetic fields produced by current-carrying wires or by spin-polarized currents, which are prone to energy dissipation through the Joule heating effect. To minimize this undesirable effect, new approaches have recently emerged in which electric currents are partly replaced with the use of electric fields, thereby decreasing the energy consumption during the switching operations.[2–6] Candidate materials

N. López-Pintó, Z. Tan, Z. Ma, E. Menéndez, J. Sort
Departament de Física
Universitat Autònoma de Barcelona
Bellaterra 08193, Spain
E-mail: jordi.sort@uab.cat
C. J. Jensen, Z. Chen, K. Liu
Physics Department
Georgetown University
Washington DC, DC 20057, USA
E-mail: kai.liu@georgetown.edu

The ORCID identification number(s) for the author(s) of this article can be found under https://doi.org/10.1002/adfm.202404487

DOI: 10.1002/adfm.202404487

C. J. Jensen
NIST Center for Neutron Research
Gaithersburg, MD 20899, USA
M. O. Liedke, M. Butterling, A. Wagner
Institute of Radiation Physics
Helmholtz-Zentrum Dresden – Rossendorf
01328 Dresden, Germany
J. Herrero-Martín
ALBA Synchrotron Light Source
Bellaterra 08290, Spain
J. Nogués, J. Sort
Institució Catalana de Recerca i Estudis Avançats (ICREA)
Pg. Lluís Companys 23, Bellaterra 08010, Spain
J. Nogués
Catalan Institute of Nanoscience and Nanotechnology (ICN2)
CSIC and BIST, Campus UAB, Bellaterra, Barcelona 08193, Spain

for voltage-controlled magnetic devices include multiferroic heterostructures,[6–8] ultra-thin metallic films and semiconductors based on electrostatic charging or carrier doping,[9,10] and materials whose magnetic properties can be tuned via redox reactions[11–13] or electric-field-triggered ion displacement (i.e., magneto-ionics).[14–20] The latter results in large non-volatile (i.e., permanent), analog and reversible changes of magnetic properties, holding potential for the development of low-energy spintronics and neuromorphic memories.[21,22]

A wide variety of magnetic functionalities can be tuned by means of magneto-ionics. For instance, reversible modifications of saturation magnetization (M_S) have been observed in many systems, often through the intercalation (or withdrawal) of O^{2-} ions in the ferromagnetic (FM) layers,[18,23–35] and, less frequently, by introducing (or removing) H^+, Li^+, OH^-, or N^{3-} ions.[22,36–42] Other remarkable effects include the regulation of the Curie temperature (T_C) in oxide systems,[29,43,44] fine-tuning of exchange bias (EB) through redox processes or proton (H^+) pumping,[11,12,45–47] reversible modification of coercivity (H_C) by up to 100%,[30] switching of the anisotropy easy axis in systems such as Co/GdO_x[16,36,48] or reversibly shifting the ferromagnetic resonance field by modulating the oxidation state of transition metals.[49,50] Interestingly, while many of these examples are based on oxidation/reduction reactions,[20] nitrogen-based magneto-ionics has been reported to induce larger changes of magnetization with lower threshold voltages, improved switching times and cyclability compared to their oxygen counterpart.[40,41] One of the current challenges in many magneto-ionic systems is the substitution of liquid electrolytes by solid electrolytes for their operation. The advantages of liquid electrolytes include avoiding pinholes and maximization of the electric field. These are hard to replicate in solid state configurations, though some soft-solid electrolytes (ionic gels) have proven successful in triggering oxygen motion.[49–51] Full-solid-state configurations are often preferred for practical electronic devices.[52,53]

Nitrogen magneto-ionics has been explored in CoN,[41,54] FeN,[54] CoFeN,[55,56] and CoMnN[40] films actuated using liquid propylene carbonate-based electrolytes. A very recent study has also shown the potential of nitrogen magneto-ionics in solid state to tune EB in Ta/MnN/CoFe/Ta stacks.[57] However, the high temperature treatment during the conventional field cooling process to establish the EB also triggered the motion of N ions toward Ta.

The objective of this study is to emulate the favorable characteristics of liquid-electrolyte gated nitrogen-based systems to develop a solid-state magneto-ionic configuration which can be controllably altered with electric fields from the as-prepared (i.e., not heat-treated) state. For this purpose, thin films of the ternary $Co_xMn_{1-x}N$ compound sandwiched between two Ta layers (Ta/$Co_xMn_{1-x}N$/Ta) have been investigated. Adding Co to the MnN was expected to decrease the bonding energy between Mn and N, therefore facilitating the electric-field-triggered nitrogen migration. The results reveal that the magneto-ionic effect scales with the Co content, leading to large voltage-driven variations of magnetization (with a non-volatile M_S increase of >100% at room temperature) for the composition with $x = 0.55$. Electron energy loss spectroscopy (EELS) mappings indicate that nitrogen ions are driven toward the Ta seed layer after gating. Additionally, the pristine sample of the same composition shows an exchange bias loop shift of 1.26 kOe, which is halved after gating. This indicates that a mixture of ferromagnetic (FM) and antiferromagnetic (AFM) phases, tunable with voltage, co-exist in these $Co_xMn_{1-x}N$ single layers. Our results are appealing for the development of solid-state magneto-ionic devices, compatible with complementary metal-oxide-semiconductor (CMOS) technology, with potential applications in new types of spintronic and magnetic memory systems.

2. Results and Discussion

2.1. Magnetic and Structural Characterization

Thin films of Ta/$Co_xMn_{1-x}N$/Ta were sputtered on top of thermally oxidized p-type Si (100) substrates (with a SiO_2 thickness of 285 nm). The $Co_xMn_{1-x}N$ thickness was nominally 50 nm, and the top and bottom Ta layers were 10 nm thick. The amount of Co corresponded to $x = 0$, 0.10, 0.15, 0.24, 0.42, and 0.55. The composition of the samples was probed through energy dispersive X-ray spectroscopy (EDX) in several regions of the films to account for homogeneity (see Table S1, Supporting Information). The samples were subsequently electrically actuated (gated) at 20 V for 1 h at room temperature (RT) using the configuration depicted in **Figure 1a**, establishing an electric field from the bottom *p*-type Si toward the top Ta. The configuration was chosen so that the SiO_2 served as the main dielectric layer. The bottom Ta layer could have also been used as the bottom electrode, but the ternary layer may become conductive depending on the N content, consequently weakening the magneto-ionic effect[58] and/or generating pinholes. The magnetic reversibility of the samples was probed by subsequent gating at −20 V for 1 h with the same configuration. However, it was only successful on the Co-richer samples with $x = 0.42$ and 0.55 (see Figure 1).

In-plane hysteresis loops were measured using a vibrating sample magnetometer (VSM) in the as-prepared (AP) and gated states, as shown in Figure 1c-h. The sample with 0 at.% Co, i.e., MnN, is anticipated to be AFM with the sputtering conditions used, which are similar to other AFM MnN studies.[59,60] This is in agreement with its magnetic signal, which is close to zero, and no changes are observed after gating. The saturation magnetization (M_S) of the AP samples increases modestly with the addition of Co. Note that the value of M_S was calculated by extrapolating the linear region of the M-H loops at high fields back to zero field. After gating at RT, a considerable increase in M_S is observed. Moreover, the voltage-driven increase of M_S is larger for higher Co contents. For instance, while the M_S of the $Co_{0.10}Mn_{0.90}N$ (i.e., $x = 0.10$) sample remains moderately low (from 7.7 emu cm^{-3} in the AP state to 10.8 emu cm^{-3} after gating), for $x = 0.55$ the M_S enhancement is more remarkable, ≈110% (15.1 emu cm^{-3} in the AP state vs 31.9 emu cm^{-3} after gating).

The precise M_S dependence with the Co atomic concentration is shown in Figure 1b. While before gating the increase in M_S with Co addition is moderate, the M_S of the gated samples scales rapidly with the Co content (from 2.3 emu cm^{-3} for 0 at.% Co up to 31.9 emu cm^{-3} for $x = 0.55$), in contrast to the gain in the AP state (from 1.2 to 15.1 emu cm^{-3} for $x = 0$ and $x = 0.55$, respectively). The M_S increase becomes particularly pronounced for $x = 0.55$, suggesting that a sufficiently high concentration of Co promotes significant magneto-ionic effects. On the other hand, the

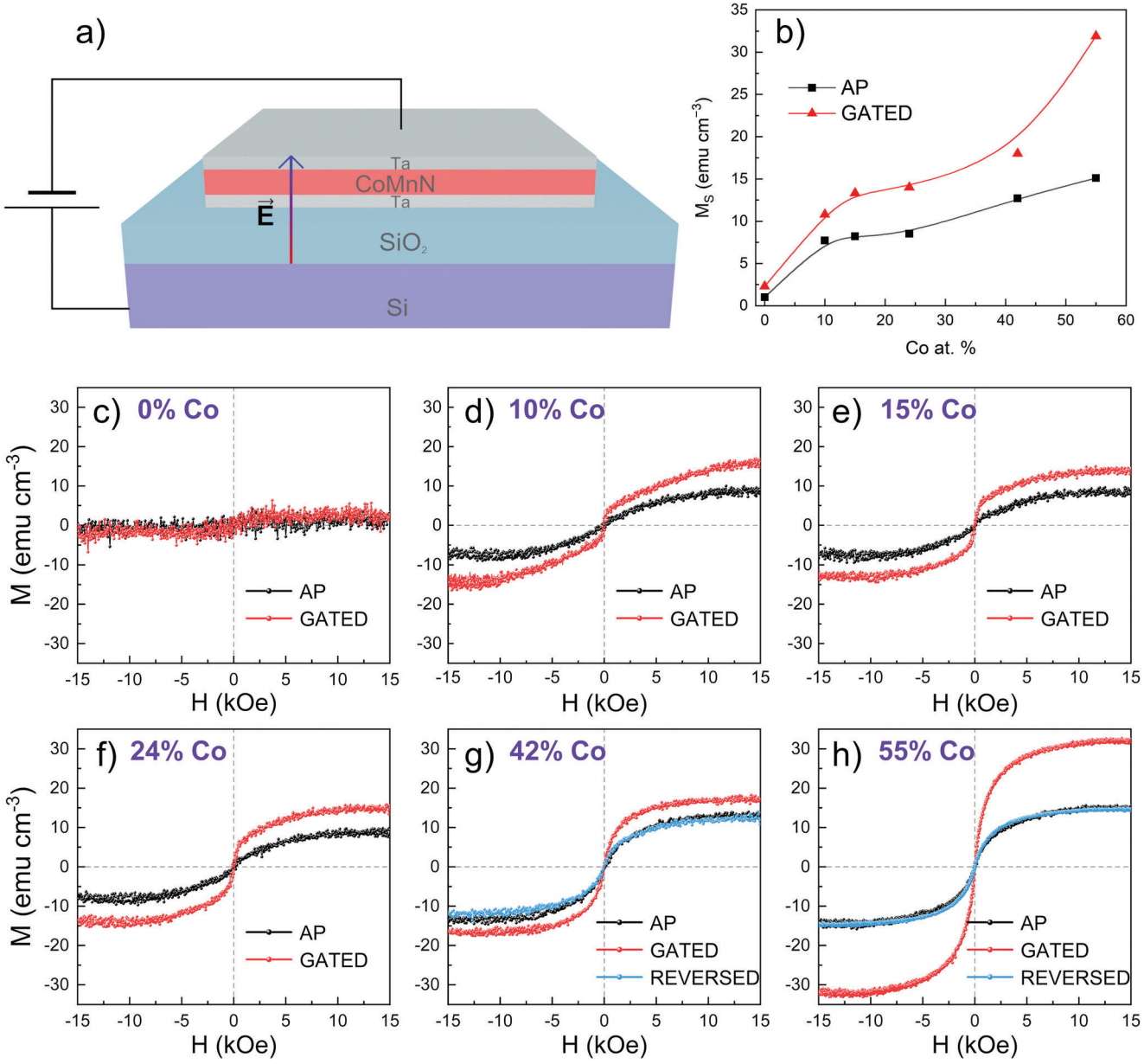

Figure 1. a) Schematic of the sample stack and the gating layout. CoMnN is a simplified notation for $Co_xMn_{1-x}N$. b) Dependence of M_S with the at.% Co for the as-prepared (AP) and gated states. c–h) Hysteresis loops at room temperature corresponding to films with Co percentages of 0 at.% (c), 10 at.% (d), 15 at.% (e), 24 at.% (f), 42 at.% (g), and 55 at.% (h), in the AP state (black curves) and after gating with +20 V for 1 h at room temperature (red curves) in the configuration shown in (a). Additionally, hysteresis loops from the reversed state, obtained after applying −20 V for 1 h, are shown in (g) and (h) (blue curves).

squareness values (M_R/M_S, where M_R is the remanent magnetization) for both states are modest, all of them between 0.05 and 0.3, and they tend to decrease as the at.% Co increases, suggesting that hysteretic properties are dominated by randomly oriented, non-interacting magnetic clusters, particularly for large x.

To better understand the progressive increase in M_S with cobalt content, X-ray diffraction (XRD) measurements were performed on the as-prepared samples, as shown in **Figure 2a**. Two main peaks are present in most of the patterns. The primary peak progressively shifts with the addition of Co, from 2θ = 42.6° (at $x = 0$), corresponding to the tetragonal MnN (002)/(200) phase,[57,59,61,62] up to 2θ = 44.6° (at x = 0.55), which matches with the orthorhombic Co_2N(021) (PDF 01-072-1368) phase.[63–65] Considering that most of the Mn_xN_y and Co_xN_y phases with the same value for x and y have similar crystallographic structures and lattice parameters (typically smaller for Co compounds), the continuous change of the ternary layer main peak suggests that the incorporation of Co in the MnN occurs through atomic substitution. Also, the proposed Co_2N is probably a $(Co,Mn)_2N$ phase with lattice parameters slightly different from those of

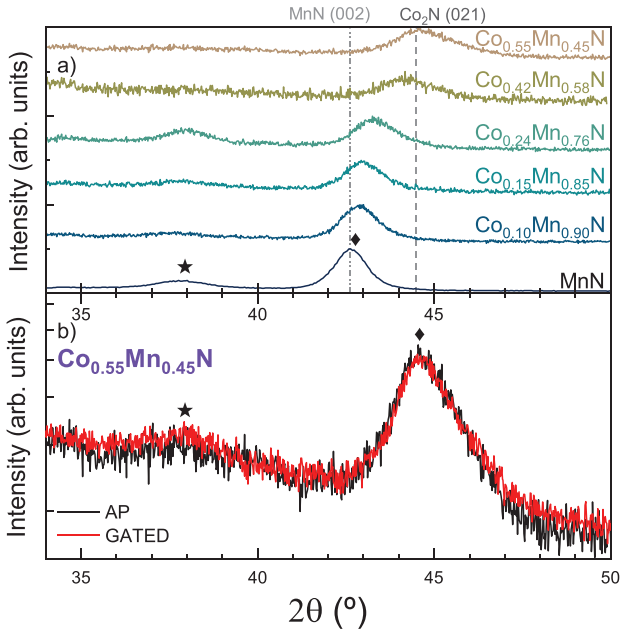

Figure 2. a) XRD patterns of $Co_xMn_{1-x}N$ layers with variable Co content from x = 0–55. b) XRD patterns of the $Co_{0.55}Mn_{0.45}N$ sample in the as-prepared (AP) and gated states. Reference lines are drawn at the angular positions of MnN and Co_2N phases as guides for the eyes. The peaks marked with a star are associated with the Ta (202), while the ones marked with a diamond are associated with the $Co_xMn_{1-x}N$.

pure Co_2N. The primary $Co_xMn_{1-x}N$ peak broadens as it shifts to higher 2θ angles, with increasing Co content (Figure 2a). This broadening occurs asymmetrically, likely caused by variations in the composition due to the presence of less nitrided phases, such as Co_3N[66] or Co_4N/Mn_4N (which have smaller lattice parameters than Co_2N), resulting from the nitrogen loss with the addition of Co. This effect can be explained by considering the dissimilar enthalpies of formation between Mn and Co. Since the enthalpy to form CoN is lower than that needed for MnN, the Mn—N bond is expected to be stronger than the Co-N one.[67] Thus, the Co incorporation is expected to weaken the metal-nitrogen bonds, facilitating nitrogen mobility and, eventually, leading to nitrogen loss. Indeed, phases such as Co_3N (FM), Co_4N (FM) or Mn_4N (ferrimagnetic, FiM) could explain the magnetism observed in the hysteresis loops discussed later, as Co_2N is reported to be AFM below 11 K.[63,64] The second, less intense peak, located $\approx 2\theta = 38°$ and marked with a star, is consistent with tetragonal Ta (202) (PDF 00-019-1290) and it is not present in all patterns. The absence of this peak could be ascribed to amorphous-like tantalum. Figure 2b shows the XRD pattern for the composition corresponding to $x = 0.55$ before and after gating. Interestingly, no major differences are identified between the patterns, indicating that the magnetization increase does not originate from major structural modifications but likely from the formation of clusters with a volume below the threshold to be probed by XRD, or by interstitial N motion.

To complement the XRD structural characterization, high-resolution transmission electron microscopy (HRTEM) images were taken for the $Co_{0.55}Mn_{0.45}N$ sample in both the AP and gated states (see Supporting Information, Figure S1). Interplanar distances corresponding to Co_2N are identified in both states. Less frequently, interplanar distances corresponding to other candidate phases are also present in both states, such as AFM MnN (002) (1.85 Å) and FiM Mn_4N (111) (2.24 Å). Additionally, interplanar distances that match FM Co_3N (111) (2.00 Å), were also found in the HRTEM images of the gated sample. Further narrowing down of the possible ferro/ferrimagnetic phases requires additional characterization, as will be described below. Note that the aforementioned phases may exist in our particular case as nitride $(Co,Mn)_xN_y$ solid-solutions.

Low-temperature magnetic hysteresis loops were recorded for the $Co_{0.55}Mn_{0.45}N$ sample using a SQUID magnetometer, before and after gating at RT, to confirm whether the AFM transition of Co_2N, expected at 11 K, was indeed observed.[63,64] **Figure 3**a,b show the loops recorded at 300, 200, 100, 50, 20, and 10 K for the AP and gated states, respectively. During the cooling process, a field of 10 kOe was applied to the sample in order to induce a shift of the hysteresis loop (i.e., EB effect[68]). The results reveal that the coercivity increases at low temperatures, and an evident EB effect appears below 30 K. By carefully inspecting these low-temperature loops, two contributions can be observed: an unbiased soft component, resembling the loops above 50 K, and a magnetically harder one which is exchange biased. After gating, the amount of soft phase contribution in the loop increases considerably, and the overall loop shift becomes less prominent. Figure 3c shows the evolution of M_S with temperature for both states. The M_S increases from 15.1 emu cm^{-3} at 300 K to 96.2 emu cm^{-3} at 10 K for the AP sample, and from 31.9 emu cm^{-3} at 300 K to 103.1 emu cm^{-3} at 10 K for the gated sample, respectively. The difference of M_S between the AP and gated states becomes less pronounced as T decreases and, below 100 K, both samples show similar M_S values. The dependence of coercivity and exchange bias of the films with temperature is shown in Figure 3d. The coercivity remains modest until 100 K, below which it starts to increase gradually. Below 50 K, it quickly ramps up, reaching 4.12 and 2.49 kOe at 10 K for the AP and gated samples, respectively. In the inset of Figure 3d, a similar trend is presented for the EB field (H_E). H_E remains zero down to 30 K, below which it rapidly increases to 1.26 kOe (AP) and 0.59 kOe (gated) at 10 K. The shape of the hysteresis loops alongside the evolution of M_S corroborates the presence of two FM components, which can be related to the two aforementioned contributions. The hard contribution, FM/FiM at room temperature, probably consists of large, ordered clusters or a layered morphology, while the soft one likely originates from small clusters. Some of these clusters are possibly small enough to be superparamagnetic, hence explaining the M_S behavior with temperature. Upon gating, new superparamagnetic sites are formed, or the size of the existing ones increases while the effect on the magnetically ordered clusters is less pronounced, with a smaller M_S enhancement.

The observation of EB in the low-temperature loops implies the coexistence of both FM and AFM phases in the $Co_{0.55}Mn_{0.45}N$ layer, as neither Ta nor TaN is magnetic. The FM phase has already been discussed, while the XRD results suggest that the AFM phase is likely $(Co,Mn)_2N$ for $x = 0.55$. From the low-temperature magnetometry measurements, a $T_N \approx 20$–30 K is established, slightly higher than the value expected for Co_2N, suggesting that the addition of Mn alters this transition temperature.

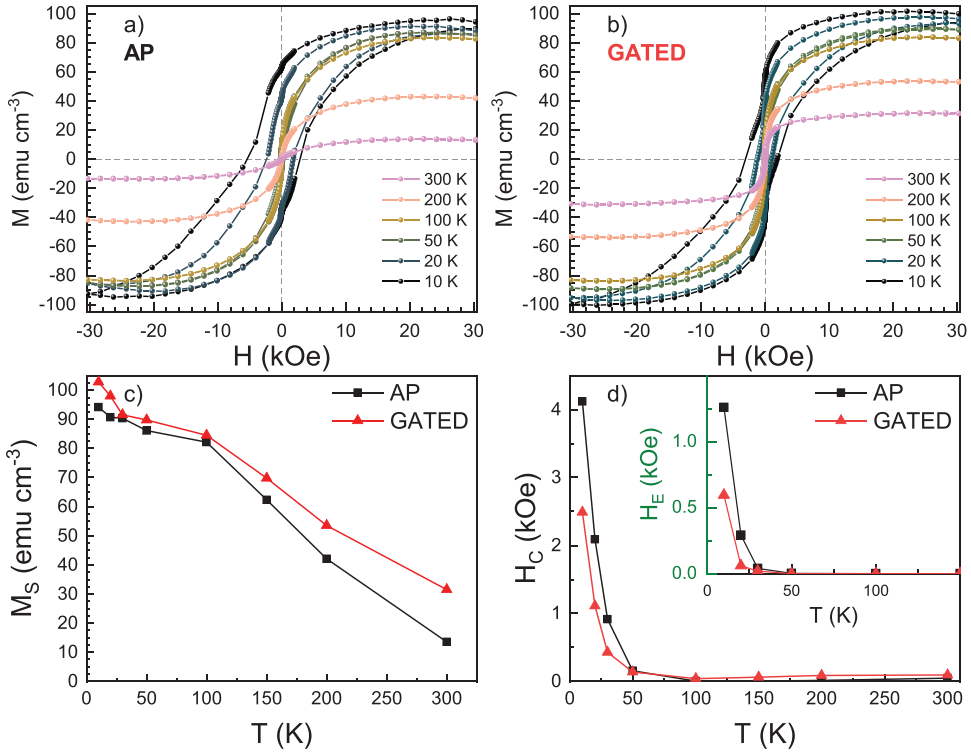

Figure 3. Hysteresis loops of the $Co_{0.55}Mn_{0.45}N$ sample from 300 to 10 K in the as-prepared (AP) a) and gated b) states. c) Dependence of the saturation magnetization with temperature in both states. d) Dependence of the coercivity and exchange bias field (H_E) (in the inset) with temperature for both states.

It has been previously shown that a solid solution of an AFM compound with a higher T_N and another with lower T_N can produce an AFM system with an intermediate T_N.[69–72] Thus, given that all known AFM phases of manganese nitrides have T_N above RT [e.g., T_N(MnN) = 660 K, $T_N(Mn_2N)$ = 301 K and $T_N(Mn_3N_2)$ = 925 K],[57,73–75] it is expected that the obtained T_N for $(Co,Mn)_2N$ is higher than that for pure Co_2N. The large EB in the AP state indicates that this AFM phase couples to clusters of FM Co_3N [or more likely $(Co,Mn)_3N$] and/or FM Co_4N or FiM Mn_4N phase [or likely a mixture such as $(Co,Mn)_4N$ as both Mn_4N and Co_4N have a cubic phase with similar lattice constants]. Given the inverse relation between the FM size and EB,[68,76] the decrease in EB could be explained by the electric field induced growth of the structures observed in the AP state. Namely, during gating the more metallic FM/FiM $(Co,Mn)_3N$ or $(Co,Mn)_4N$ component grows at the expense of the $(Co,Mn)_2N$. In addition, during the gating, new small clusters of FM/FiM $(Co,Mn)_3N$ or $(Co,Mn)_4N$ could also be formed from the $(Co,Mn)_2N$ layer. The fact that these small clusters are not exchange biased, could be related to the minimal size required to induce EB in small clusters.[77] Note that these assumptions are reasonable in the context of our experiment, provided that voltage induces a loss of N in the $Co_xMn_{1-x}N$ layer.

2.2. Nitrogen Migration Mechanisms

With the configuration depicted in Figure 1a, upon application of positive voltage, N ions are expected to diffuse toward the bottom Ta layer. To elucidate the redistribution of nitrogen across the heterostructure, electron energy loss spectroscopy (EELS) and depth-resolved variable energy positron annihilation lifetime spectroscopy (VEPALS) were used.

The EELS maps for oxygen (green), nitrogen (red), cobalt (blue), and manganese (pink) $Co_{0.55}Mn_{0.45}N$ lamellae are shown in **Figure** 4a,b for the AP and gated states, respectively, alongside their corresponding scanning transmission electron microscopy/high-angle annular dark-field (STEM/HAADF) image. Yellow dashed lines are drawn as guides to the eye to separate the different layers in the structure. The boundaries were set considering the contrast in brightness between layers and the elements present in them. The maps are rather homogeneous, with no obvious ion channels (in contrast to oxide-based systems[24,41]). However, no clear nitrogen diffusion front can be observed, unlike that seen in liquid-electrolyte gated nitrides,[22,41] indicating that in N-based solid-state gating the observed effects are more subtle. In addition, traces of N are observed in both Ta layers before and after gating. The top Ta is also partially oxidized, resulting in lower brightness compared to the bottom Ta. The STEM/HAADF image displays a blue solid line, across which an EELS scan was performed. The normalized intensity of the nitrogen and the brightness alongside the scan are plotted in Figure 4c for both states. The nitrogen intensity was normalized to the Mn signal from the ternary layer, which had an intensity comparable in the maps from both states (AP and gated) and was uniform along the film. From a simple inspection, the changes in the nitrogen distribution are not evident both in the

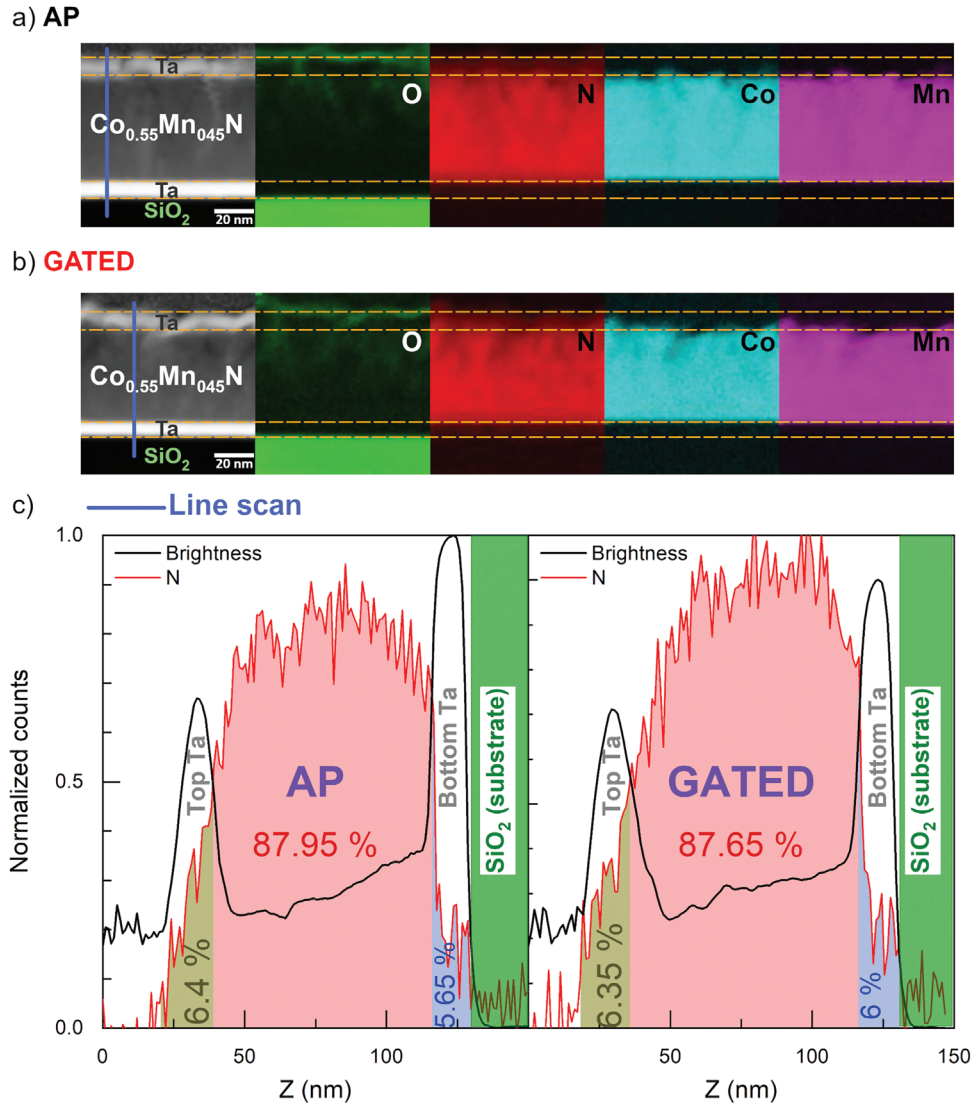

Figure 4. From left to right, STEM/HAADF image and EELS mapping of O (green), nitrogen (red), cobalt (blue) and manganese (pink) for the as-prepared (AP) a) and gated b) states of the $Co_{0.55}Mn_{0.45}N$ sample. A line has been drawn in the STEM image over which an EELS scan was performed. The results for the brightness and the nitrogen signal of the line scan are shown in (c).

maps or the line scans, although the overall N line scan appears to be slightly shifted after gating (with the maximum N signal at the bottom half of the $Co_{0.55}Mn_{0.45}N$ layer). An in-depth statistical analysis was performed to assess the nitrogen migration throughout the film. In particular, the area under the N curve in the line scans from Figure 4c was integrated, which is related to the nitrogen content of the layer. The analysis reveals that the area of the N signal in the $Co_{0.55}Mn_{0.45}N$ layer is 0.3% larger in the AP sample compared to the gated sample, contrary to what occurs in the bottom seed Ta layer, where the N content increases slightly after gating. A similar trend was observed from an in-depth analysis of the EELS nitrogen map, where the mean intensity of the $Co_xMn_{1-x}N$ layer is higher in the AP state compared to the gated, and in contrast to the increase in N content in the Ta seed layer after gating (see Figure S2 and Table S2, Supporting Information). These observations are consistent with the expected N-ion diffusion behavior after gating the sample, i.e., nitrogen migrating toward the bottom part of the structure. Previous studies on thermally annealed Ta/MnN/CoFe/Ta also had difficulties elucidating the N redistribution along their heterostructure, as the N variation in the EELS signal was non-existent. Nonetheless, the moderate changes in the N distribution along the layers produced a substantial increase of the EB of the system.[57] Likewise, in the current case, minor changes in the N content across the $Co_{0.55}Mn_{0.45}N$ layer led to significant changes in its magnetic properties.

The defect structure of the $Co_{0.55}Mn_{0.45}N$ sample was also characterized, before and after gating, through VEPALS to shed further light on the ion migration mechanisms. The technique enables the acquisition of positron lifetimes which are proportional to defect sizes (i.e., the larger the open volume, the longer the positron lifetime) and their relative intensities reflect, to some

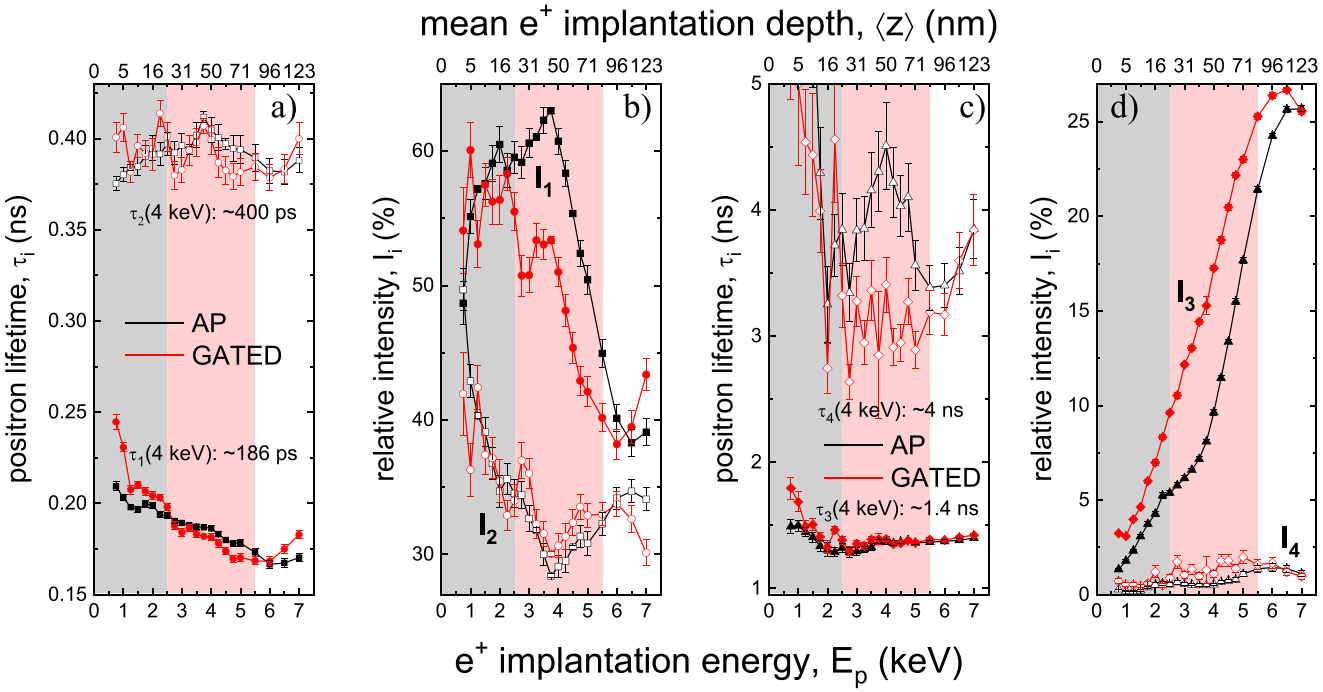

Figure 5. Depth-resolved variable energy positron annihilation lifetime spectroscopy (VEPALS) results for the $Co_{0.55}Mn_{0.45}N$ sample in the as-prepared (AP) and gated states, represented by black and red symbols, respectively. a) shows the first and second lifetime components (τ_1 and τ_2, respectively) and b) their relative intensity (I_1 and I_2, respectively). c) shows the third and fourth lifetime components (τ_3 and τ_4, respectively) and d) their relative intensity (I_3 and I_4). The grey and light red shaded areas represent the top Ta layer and the adjacent $Co_{0.55}Mn_{0.45}N$ layers, respectively.

extent, the concentration of each defect (see the Experimental Section for further details).[78,79] The results of VEPALS are shown in **Figure 5**, where the first three components of positron lifetime can be distinguished: τ_1, τ_2, and τ_3. The lifetime components are consistent with small vacancy clusters, grain boundaries (i.e., large vacancy clusters) and pores (of ≈0.5 nm in diameter), respectively (see Table S3, Supporting Information). Larger pores are represented by the fourth component (τ_4) and, as seen in Figure 5d, are only residual since the relative intensity falls below 2% across the entire heterostructure for both AP and gated samples. Remarkably, τ_1, τ_2, and τ_3 do not significantly change upon gating (note that black and red symbols largely overlap), indicating that the defect sizes remain unaltered. The positron lifetimes recorded for $E_p = 4$ keV (hence for depth of ≈50 nm) of $\tau_1 \approx 186$ ps, $\tau_2 \approx 400$ ps, correspond to the density functional theory (DFT) calculated defect sizes of between 1 and 2, and ≈30 vacancies, respectively (see Table S3, Supporting Information),[58] whereas, $\tau_3 \approx 1400$ ps and $\tau_4 \approx 3100$–4500 ps are much longer and represent micropores of a size ≈ 0.47 nm and 0.6–0.9 nm, respectively.[80] Conversely, relative intensities I_1, I_3, and I_4 become strongly affected after biasing: I_1 decreases, while I_3 and I_4 increase across the whole heterostructure. This indicates the formation of micro-pores at the expense of small vacancy clusters, confirming mild ion migration processes upon voltage. This compensation seems to be accentuated in the upper region of the $Co_{0.55}Mn_{0.45}N$ layer, close to the interface with Ta. For instance, I_1(AP) grows larger until the positron implantation energy surpasses 3.75 keV (≈45 nm deep), while the I_1(gated) quickly decreases until 2.75 keV (≈27 nm), and, after remaining constant ≈51%, the intensity further decreases in a similar fashion to I_1(AP) after 3.75 keV. Similarly, I_3 behaves differently close to the interface for the AP state compared to that after gating. At ≈45 nm, 3.75 keV, both I_3(AP) and I_3(gated) start increasing at the same pace.

Therefore, the VEPALS results further support that the gating effect is rather subtle, and the effects are more pronounced close to the upper interface. The overall crystalline structure remains rather unaffected by the N rearrangement, as seen from the XRD patterns, indicating that the amount of nitrogen that migrates is not enough to distort the film's lattice and suggesting that the topmost layers are the most affected by the nitrogen displacement (or loss).

2.3. Advanced Spectroscopy Analysis

To further corroborate which phases are present in the $Co_{0.55}Mn_{0.45}N$ sample, X-ray absorption spectroscopy (XAS) was carried out before and after gating. The total electron yield (TEY) XAS spectra of Co and Mn $L_{2,3}$ edges at 300 K and base temperature (<10 K) are shown in **Figure 6**, together with their corresponding X-ray magnetic circular dichroism (XMCD) signal. As can be seen in the figure, all TEY-XAS spectra show fine structure, indicating that Co and Mn are in a non-metallic state. This is consistent with the energy of the *K*-edge XAS of Co_3N and Co_2N, which indicates that the effective valence state of Co in Co_3N and Co_2N would be between Co^{1+} and Co^{2+}.[81,82] In contrast, the *L*-edge XAS Co_4N has a more metallic character, which would lead to a rather featureless XAS in the L_3 edge of Co.[83] The Mn *L*-edge XAS of the $Co_{0.55}Mn_{0.45}N$ samples also show some fine structure,

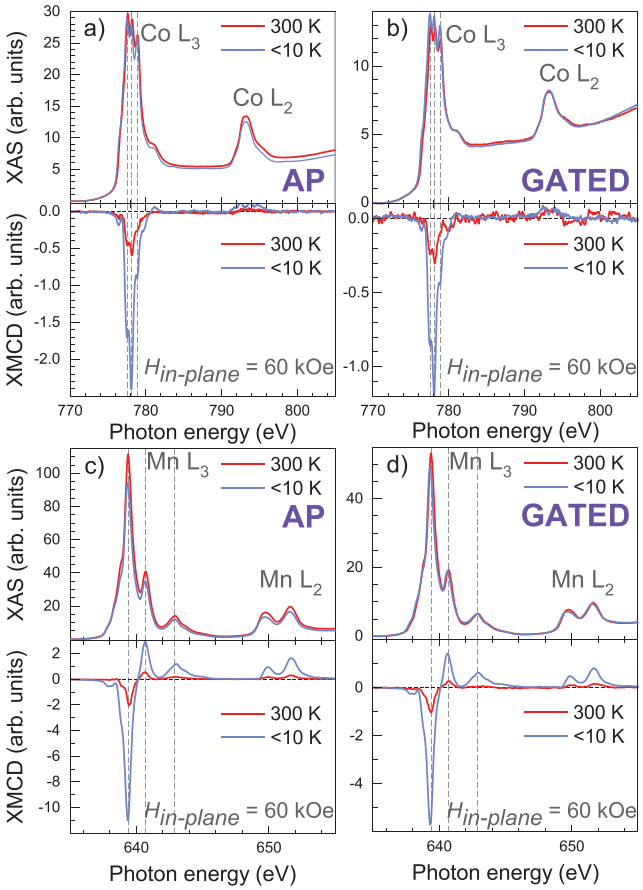

Figure 6. $Co_{0.55}Mn_{0.45}N$ XAS and XMCD spectra of the Co $L_{2,3}$ a,b) and Mn $L_{2,3}$ c,d) edges for the as-prepared (AP) (a,c) and gated (b,d) states at 300 K (red curve) and base temperature < 10 K (blue curve). XMCD spectra were recorded with an in-plane magnetic field of 60 kOe. Dashed vertical lines are drawn as eye-guides to the positions of the peaks found in the L_3 edge.

which may indicate a higher Mn valence state than that for Mn_4N and closer to Mn^{2+}.[84–86] Interestingly, the shape of the Co and Mn TEY-XAS spectra barely changes after gating, indicating that there is no drastic change in the valence state of the transition metals from the phases present in the film after the voltage is applied, neither when decreasing the temperature below T_N, in agreement with the other characterization techniques.

The single peak in the Co XMCD *L*-edge spectra (Figure 6a,b) indicates that the order of the Co ions is FM. In contrast, the Mn XMCD *L*-edge spectra (Figure 6c,d) show positive and negative peaks, suggesting a FiM arrangement of the Mn ions. Note that different magnetic order in the Mn and Co ions is in concordance with the different magnetic order observed in Mn- and Co-based nitrides.[83] The intensity increase of the XMCD signals between 300 K and low temperature for both Mn and Co indicates that the magnetization increases substantially as the temperature is lowered, as observed from magnetometry measurements.

Interestingly, there are no apparent changes in the shape of the XMCD spectra of the sample before and after gating, eventually differing from what is observed in magnetometry. The magnetic moment per atom of Co and Mn before and after gating were extracted from the XMCD signal at 300 K and low temperature using the sum rules,[87,88] and the results are summarized in **Table 1**. It is worth noting that many of the atoms in the $Co_{0.55}Mn_{0.45}N$ layer do not contribute to the ferro/ferrimagnetism in the film, which leads to rather low moments extracted from the XMCD analysis. The total Co magnetic moment per atom at 300 K doubles after gating (from 0.06 μ_B/atom to 0.12 μ_B/atom). Yet, the increase of M_S observed after gating slightly exceeds 100%, as shown in the magnetometry section. This additional gain can be related to the increment of the total Mn magnetic moment after gating, from 0.09 μ_B/atom to 0.12 μ_B/atom. At low temperatures, the magnetic moment remains largely unaffected after gating, 0.25 μ_B/atom for Co and 0.55 μ_B/atom for Mn, consistent with the magnetometry results.

Table 1. Obtained Co and Mn magnetic moments per atom from applying the sum-rules to the XMCD data for both states [as-prepared (AP) and gated] at the two temperatures measured (300 K and base temperature, <10 K). The total moment corresponds to the sum of the orbital and spin moments.

Element	State [AP/Gated]	Temperature [K]	m_{TOT} [μ_B/atom]
Co	AP	300	0.06 ± 0.01
Mn	AP	300	0.09 ± 0.01
Co	AP	<10	0.25 ± 0.06
Mn	AP	<10	0.54 ± 0.06
Co	Gated	300	0.12 ± 0.01
Mn	Gated	300	0.12 ± 0.01
Co	Gated	<10	0.25 ± 0.02
Mn	Gated	<10	0.55 ± 0.04

The fact that the shape of the XMCD spectra does not change upon gating may suggest that rather than reducing the magnetic $(Co,Mn)_3N$ toward a more metallic FM phase [e.g., Co or $(Co,Mn)_4N$], more $(Co,Mn)_3N$ is generated from the AFM $(Co,Mn)_2N$ phase. Nevertheless, apart from Mn in a $(Co,Mn)_3N$ phase, the magnetic moment from Mn could also originate from uncompensated Mn_2N spins due to nitrogen deficiency[75] (although this type of contribution is typically much weaker than FM or FiM signals) or the presence of FiM phases such as Mn_4N[83] in regions with a larger amount of nitrogen vacancies, as most of the other nitride phases of Mn are known to be paramagnetic or AFM at RT.[61]

Therefore, XAS and XMCD results somewhat constrain the number of possible phases mentioned in previous sections. The fine structure seen in the XAS-TEY spectra excludes the possibility of highly metallic phases such as metallic Co, Mn or CoMn alloys. Consequently, $(Co,Mn)_3N$ (Co_3N with Mn substitutions, as Mn_3N is not a stable phase) seems the most probable candidate to explain the magnetic signal of the $Co_{0.55}Mn_{0.45}N$ films. Phases such as Mn_4N (FiM) or uncompensated spins in Mn_2N cannot be completely discarded, since the XMCD signal indicates a FiM ordering of Mn.

In contrast to the TEY-XMCD results (sensitive to the topmost layers), the fluorescence yield (FY)-XMCD, which is sensitive to the whole film (see Figure S3, Supporting Information), exhibits little changes to the spectra after gating, implying that most of the magnetic modifications occur within the top layers of the film,

in agreement with the VEPALS results. Note that the difference in shape between the absorption and XMCD spectra in the TEY and FY are probably due to the self-absorption effects in the FY measurements. Thus, from the FY- XAS or XMCD it is complex to extract information concerning the valence states of both Co and Mn.

3. Conclusion

In summary, a series of Ta/$Co_xMn_{1-x}N$/Ta heterostructures were deposited by sputtering (x = 0–0.55) and afterwards electrically manipulated (gated) at RT using a solid-state configuration to induce a N redistribution inside the samples. In the as-prepared (AP) state, the magnetic signal of the ternary layer moderately increases with the amount of Co. For sufficiently high Co contents, after positive gating, the magnetic signal of the samples is enhanced, as M_S increases from 15.1 to 31.9 emu cm^{-3} in the case of x = 0.55. The voltage treatment also induces changes in the hysteresis loops at low temperatures. In particular, the $Co_{0.55}Mn_{0.45}N$ sample exhibits an exchange bias effect below 30 K, which can also be tuned (≈50% at 10 K) by applying an electric field at RT. The phases responsible for the observed magnetic behavior are pinpointed using XRD, HRTEM and XAS. The most probable scenario is a matrix of $(Co,Mn)_2N$ (AFM, T_N = 30 K) with embedded superparamagnetic clusters of $(Co,Mn)_3N$ (FM) or $(Co,Mn)_4N$ (FiM), with a blocking temperature ≈100 K. After gating, the evidence points to more and/or larger magnetic clusters being formed from the $(Co,Mn)_2N$ matrix, allowing the possibility to tune the magnetic phases with voltage. These results demonstrate the feasibility of solid-state nitrogen magneto-ionics in $Co_xMn_{1-x}N$ films, which is appealing for applications in low-power spintronic and memory devices by avoiding energy losses from heat dissipation.

4. Experimental Section

Sample Preparation: A series of thin film heterostructures comprising Ta seed/ $Co_xMn_{1-x}N$/ Ta cap layers were grown through direct current (DC) magnetron sputtering on top of thermally oxidized (285 nm SiO_2) p-type Si substrates. The thickness of the ternary layer was 50 nm nominally, while the Ta seed and cap layers were 10 nm thick. The deposition was assisted by a shadow mask, in order to pattern the films in areas of 5 mm × 5 mm. Before deposition, a base pressure better than 5 × 10^{-8} Torr was always reached. All 10 nm Ta layers were deposited at room temperature (RT) and 3 mTorr in a full Ar atmosphere, using 50 W DC power. The ternary layer was reactively co-sputtered from Co (99.99%) and Mn (99.99%) metallic targets in a 1:1 Ar:N_2 atmosphere. The working pressure was set to 2.5 mTorr and the substrate temperature at RT. The Co content was varied from 0 to 55 at.%. The amount of Co included in the layers was controlled either by changing the power applied to Co (from 25 W up to 50 W) or changing the Co gun's geometry (see Table S1, Supporting Information), as plasma could not be lit below 20 W with the mentioned depositing conditions.

Magnetic Measurements: In-plane magnetic characterization of the samples was performed using a LakeShore 8600 series vibrating sample magnetometer (VSM). The VSM hysteresis loops were recorded at RT with a maximum applied field of 19 kOe. All samples were measured in the as-prepared (AP) state and after undergoing an ex situ treatment of +20 V during 1 h (GATED sample) with an Agilent B2902A power supply. The bottom contact was made by scratching the oxidized SiO_2 and pasting a small piece of indium on the scratch to ensure good contact with the doped Si. The top contact was directly placed on the conductive Ta. Complementary low-temperature measurements were acquired for the $Co_{0.55}Mn_{0.45}N$ sample in the AP and GATED states using a superconducting quantum interference device (SQUID) magnetometer (Quantum Design MPMS3). To induce EB, the sample was cooled in a 10 kOe field from 300 K to a measurement temperature of 300, 200, 150, 100, 50, 30, 20, and 10 K. In-plane hysteresis loops were then measured at each temperature.

Structural and Compositional Analysis: The Co and Mn contents in all layers were quantified through energy dispersive X-ray spectroscopy (EDX). The structural characterization was performed by X-ray diffraction, using a Malvern-Panalytical X'Pert3 MRD system with Cu K_α radiation. The θ–2θ scans were measured in the 2θ range from 30° to 55° using a PixCel^{1D} line detector with a 0.02° step size and total integration time of 200 s. Additionally, cross-section lamellae from the $Co_{0.55}Mn_{0.45}N$ films in the AP and GATED states were prepared by focused ion beam (FIB). They were subsequently observed by high resolution transmission electron microscopy (HRTEM) and electron energy loss spectroscopy (EELS) on a TECNAI F20 HRTEM/STEM microscope operated at 200 kV.

X-ray absorption spectroscopy (XAS) and x-ray magnetic circular dichroism (XMCD) measurements at the Co and Mn $L_{2,3}$ edges were carried out at the BOREAS beamline of the ALBA synchrotron in Barcelona, Spain[89] for the $Co_{0.55}Mn_{0.45}N$ sample in the AP and GATED states. The spectra were acquired at RT and <10 K (base temperature) in a grazing angle (60° to the sample normal) in total electron yield (TEY) and partial fluorescence yield (PFY) under high vacuum conditions (10^{-7} Torr). The subtraction of the XAS signal between spectra recorded at opposite incoming beam helicities, with an in-plane applied field of 60 kOe, resulted in the XMCD spectra at the same edges.

Defect characterization by variable energy positron annihilation lifetime spectroscopy (VEPALS) measurements were conducted for the $Co_{0.55}Mn_{0.45}N$ sample in the as-prepared and gated states at the Monoenergetic Positron Source (MePS) beamline at Helmholtz-Zentrum Dresden – Rossendorf (Germany)[90] using a digital lifetime $CrBr_3$ scintillator detector, coupled to a Hamamatsu R13089-100 photomultiplier and employing a ADQ14DC-2X digitizer from SPDevices.[91] A conventional lifetime spectrum N(t) was described by $N(t) = \Sigma(1/\tau_i)I_i \exp(-t/\tau_i)$, where τ_i and I_i are the positron lifetime and intensity of the i-th component, respectively ($\Sigma I_i = 1$). All the spectra were deconvoluted using a non-linear least-squares fitting method employed within the fitting software package PALSfit[92] into four discrete lifetime components, which directly evidence localized annihilation at four different defect types (or sizes: τ_1, τ_2, τ_3, and τ_4). The corresponding relative intensities primarily reflect the concentration of each defect type (size) as long as the size of compared defects was in a similar range. Broadly, positron lifetime was directly proportional to defects size, i.e., the larger the open volume is, the lower probability there was for positrons to be annihilated with electrons, and hence the longer positron lifetime.[78,79] The positron lifetime and its intensity have been probed as a function of positron implantation energy E_P or, in other words, implantation depth (thickness). A mean positron implantation depth ⟨z⟩ (given in nm) can be approximated using a simple material density ρ = 6.83 g cm^{-3} dependent formula as $\langle z \rangle\ (\text{nm}) = \frac{36}{\rho(\frac{g}{cm^3})} E_P(\text{keV})^{1,62}$.[93]

DFT calculations of the positron lifetimes for different possible defect configurations were performed employing the so-called atomic superposition technique (ATSUP).[94] The electron-positron correlations were treated according to Boroński–Nieminen.[95] For simplicity, the $Co_{0.55}Mn_{0.45}N$ was approximated to CoN for these calculations.

Supporting Information

Supporting Information is available from the Wiley Online Library or from the author.

Acknowledgements

N.L.-P. and C.J.J. contributed equally to this work. Financial support from the European Research Council (2021-ERC-Advanced REMINDS

Grant N° 101054687), the Spanish Government (PID2020-116844RB-C21, PDC2021-121276-C31 and the MCIN/AEI/10.13039/501100011033 & "European Union NextGenerationEU/PRTR" grant CNS2022-135230) and the Generalitat de Catalunya (2021-SGR-00651) is acknowledged. Work at Georgetown University has been supported by the US NSF (ECCS-2151809) and AFOSR (FA9550-23-1-0497). The acquisition of a Magnetic Property Measurements System (MPMS3), which was used in this investigation was supported by the US NSF-MRI (DMR-1828420). Parts of this research were carried out at ELBE at the Helmholtz-Zentrum Dresden – Rossendorf e. V., a member of the Helmholtz Association. The authors would like to thank the facility staff (Eric Hirschmann) for his assistance. E.M. is a Serra Húnter Fellow. ICN2 is funded by the CERCA programme/Generalitat de Catalunya. The ICN2 is supported by the CEX2021-001214-S grant funded by MCIN/AEI/10.13039/501100011033.

Conflict of Interest

The authors declare no conflict of interest.

Data Availability Statement

The data that support the findings of this study are available from the corresponding author upon reasonable request.

Keywords

exchange bias, magnetoelectricity, magneto-ionics, nitrogen diffusion, ternary nitride compound, voltage control of magnetism (VCM)

Received: March 14, 2024
Revised: April 23, 2024
Published online:

[1] N. Jones, *Nature* **2018**, *561*, 163.
[2] H. Ohno, D. Chiba, F. Matsukura, T. Omiya, E. Abe, T. Dietl, Y. Ohno, K. Ohtani, *Nature* **2000**, *408*, 944.
[3] T. Maruyama, Y. Shiota, T. Nozaki, K. Ohta, N. Toda, M. Mizuguchi, A. A. Tulapurkar, T. Shinjo, M. Shiraishi, S. Mizukami, Y. Ando, Y. Suzuki, *Nat. Nanotechnol.* **2009**, *4*, 158.
[4] F. Xiu, Y. Wang, J. Kim, A. Hong, J. Tang, A. P. Jacob, J. Zou, K. L. Wang, *Nat. Mater.* **2010**, *9*, 337.
[5] W. G. Wang, M. Li, S. Hageman, C. L. Chien, *Nat. Mater.* **2011**, *11*, 64.
[6] J. T. Heron, J. L. Bosse, Q. He, Y. Gao, M. Trassin, L. Ye, J. D. Clarkson, C. Wang, J. Liu, S. Salahuddin, D. C. Ralph, D. G. Schlom, J. Íñiguez, B. D. Huey, R. Ramesh, *Nature* **2014**, *516*, 370.
[7] S. M. Wu, S. A. Cybart, P. Yu, M. D. Rossell, J. X. Zhang, R. Ramesh, R. C. Dynes, *Nat. Mater.* **2010**, *9*, 756.
[8] C. Thiele, K. Dörr, O. Bilani, J. Rödel, L. Schultz, *Phys. Rev. B* **2007**, *75*, 054408.
[9] W. Lin, N. Vernier, G. Agnus, K. Garcia, B. Ocker, W. Zhao, E. E. Fullerton, D. Ravelosona, *Nat. Commun.* **2016**, *7*, 13532.
[10] D. Hayakawa, A. Obinata, K. Miwa, S. Ono, T. Hirai, T. Koyama, D. Chiba, *AIP Adv.* **2016**, *6*, 115305.
[11] J. Zehner, R. Huhnstock, S. Oswald, U. Wolff, I. Soldatov, A. Ehresmann, K. Nielsch, D. Holzinger, K. Leistner, *Adv. Electron. Mater.* **2019**, *5*, 1900296.
[12] D. A. Gilbert, J. Olamit, R. K. Dumas, B. J. Kirby, A. J. Grutter, B. B. Maranville, E. Arenholz, J. A. Borchers, K. Liu, *Nat. Commun.* **2016**, *7*, 11050.
[13] P. D. Murray, D. A. Gilbert, A. J. Grutter, B. J. Kirby, D. Hernández-Maldonado, M. Varela, Z. E. Brubaker, W. L. N. C. Liyanage, R. V. Chopdekar, V. Taufour, R. J. Zieve, J. R. Jeffries, E. Arenholz, Y. Takamura, J. A. Borchers, K. Liu, *ACS Appl. Mater. Interfaces* **2020**, *12*, 4741.
[14] C. Navarro-Senent, A. Quintana, E. Menéndez, E. Pellicer, J. Sort, *APL Mater.* **2019**, *7*, 030701.
[15] C. Song, B. Cui, F. Li, X. Zhou, F. Pan, *Prog. Mater. Sci.* **2017**, *87*, 33.
[16] U. Bauer, L. Yao, A. J. Tan, P. Agrawal, S. Emori, H. L. Tuller, S. Van Dijken, G. S. D. Beach, *Nat. Mater.* **2015**, *14*, 174.
[17] D. A. Gilbert, A. J. Grutter, E. Arenholz, K. Liu, B. J. Kirby, J. A. Borchers, B. B. Maranville, *Nat. Commun.* **2016**, *7*, 12264.
[18] C. Bi, Y. Liu, T. Newhouse-Illige, M. Xu, M. Rosales, J. W. Freeland, O. Mryasov, S. Zhang, S. G. E. Te Velthuis, W. G. Wang, *Phys. Rev. Lett.* **2014**, *113*, 267202.
[19] Q. Wang, Y. Gu, C. Chen, F. Pan, C. Song, *J. Phys. Chem. Lett.* **2022**, *13*, 10065.
[20] M. Nichterwitz, S. Honnali, M. Kutuzau, S. Guo, J. Zehner, K. Nielsch, K. Leistner, *APL Mater.* **2021**, *9*, 030903.
[21] R. Mishra, D. Kumar, H. Yang, *Phys. Rev. Appl.* **2019**, *11*, 054065.
[22] Z. Tan, J. de Rojas, S. Martins, A. Lopeandia, A. Quintana, M. Cialone, J. Herrero-Martín, J. Meersschaut, A. Vantomme, J. L. Costa-Krämer, J. Sort, E. Menéndez, *Mater. Horiz.* **2022**, *10*, 88.
[23] Z. Tan, Z. Ma, L. Fuentes, M. O. Liedke, M. Butterling, A. G. Attallah, E. Hirschmann, A. Wagner, L. Abad, N. Casañ-Pastor, A. F. Lopeandia, E. Menéndez, J. Sort, *ACS Nano* **2023**, *17*, 6973.
[24] C. Navarro-Senent, A. Quintana, E. Isarain-Chávez, E. Weschke, P. Yu, M. Coll, E. Pellicer, E. Menéndez, J. Sort, *ACS Appl. Mater. Interfaces* **2020**, *12*, 14484.
[25] J. de Rojas, A. Quintana, A. Lopeandía, J. Salguero, J. L. Costa-Krämer, L. Abad, M. O. Liedke, M. Butterling, A. Wagner, L. Henderick, J. Dendooven, C. Detavernier, J. Sort, E. Menéndez, *Adv. Funct. Mater.* **2020**, *30*, 2003704.
[26] S. Robbennolt, E. Menéndez, A. Quintana, A. Gómez, S. Auffret, V. Baltz, E. Pellicer, J. Sort, *Sci. Rep.* **2019**, *9*, 10804.
[27] K. Leistner, J. Wunderwald, N. Lange, S. Oswald, M. Richter, H. Zhang, L. Schultz, S. Fähler, *Phys. Rev. B* **2013**, *87*, 224411.
[28] Q. Zhang, X. Luo, L. Wang, L. Zhang, B. Khalid, J. Gong, H. Wu, *Nano Lett.* **2016**, *16*, 583.
[29] Y. N. Yan, X. J. Zhou, F. Li, B. Cui, Y. Y. Wang, G. Y. Wang, F. Pan, C. Song, *Appl. Phys. Lett.* **2015**, *107*, 122407.
[30] S. Robbennolt, A. Quintana, E. Pellicer, J. Sort, *Nanoscale* **2018**, *10*, 14570.
[31] X. Zhu, J. Zhou, L. Chen, S. Guo, G. Liu, R. W. Li, W. D. Lu, *Adv. Mater.* **2016**, *28*, 7658.
[32] F. Zhang, Z. Li, Q. Xia, Q. Zhang, C. Ge, Y. Chen, X. Li, L. Zhang, K. Wang, H. Li, L. Gu, S. Yan, G. X. Miao, Q. Li, *Matter* **2021**, *4*, 3605.
[33] S. Dasgupta, B. Das, Q. Li, D. Wang, T. T. Baby, S. Indris, M. Knapp, H. Ehrenberg, K. Fink, R. Kruk, H. Hahn, *Adv. Funct. Mater.* **2016**, *26*, 7507.
[34] D. A. Gilbert, A. J. Grutter, P. D. Murray, R. V. Chopdekar, A. M. Kane, A. L. Ionin, M. S. Lee, S. R. Spurgeon, B. J. Kirby, B. B. Maranville, A. T. N'Diaye, A. Mehta, E. Arenholz, K. Liu, Y. Takamura, J. A. Borchers, *Phys. Rev. Mater.* **2018**, *2*, 104402.
[35] A. Quintana, E. Menéndez, M. Liedke, M. Butterling, A. Wagner, V. Sireus, P. Torruella, S. Estradé, F. Peiró, J. Dendooven, C. Detavernier, P. D. Murray, D. A. Gilbert, K. Liu, E. Pellicer, J. Nogués, J. Sort, *ACS Nano* **2018**, *12*, 10291.
[36] A. J. Tan, M. Huang, C. O. Avci, F. Büttner, M. Mann, W. Hu, C. Mazzoli, S. Wilkins, H. L. Tuller, G. S. D. Beach, *Nat. Mater.* **2019**, *18*, 35.
[37] A. J. Tan, M. Huang, S. Sheffels, F. Büttner, S. Kim, A. H. Hunt, I. Waluyo, H. L. Tuller, G. S. D. Beach, *Phys. Rev. Mater.* **2019**, *3*, 064408.

[38] M. Ameziane, R. Rosenkamp, L. Flajšman, S. van Dijken, R. Mansell, *Appl. Phys. Lett.* **2023**, *122*, 232401.
[39] M. Ameziane, R. Mansell, V. Havu, P. Rinke, S. Van Dijken, *Adv. Funct. Mater.* **2022**, *32*, 2113118.
[40] Z. Tan, S. Martins, M. Escobar, J. De Rojas, F. Ibrahim, M. Chshiev, A. Quintana, A. Lopeandia, J. L. Costa-Krämer, E. Menéndez, J. Sort, *ACS Appl. Mater. Interfaces* **2022**, *14*, 44581.
[41] J. de Rojas, A. Quintana, A. Lopeandía, J. Salguero, B. Muñiz, F. Ibrahim, M. Chshiev, A. Nicolenco, M. O. Liedke, M. Butterling, A. Wagner, V. Sireus, L. Abad, C. J. Jensen, K. Liu, J. Nogués, J. L. Costa-Krämer, E. Menéndez, J. Sort, *Nat. Commun.* **2020**, *11*, 5871.
[42] A. Quintana, A. A. Firme, C. J. Jensen, D. Zheng, C. Liu, X. Zhang, K. Liu, *J. Mater. Chem. C* **2022**, *10*, 17145.
[43] B. Cui, C. Song, G. Wang, Y. Yan, J. Peng, J. Miao, H. Mao, F. Li, C. Chen, F. Zeng, F. Pan, *Adv. Funct. Mater.* **2014**, *24*, 7233.
[44] K. Shimamura, D. Chiba, S. Ono, S. Fukami, N. Ishiwata, M. Kawaguchi, K. Kobayashi, T. Ono, *Appl. Phys. Lett.* **2012**, *100*, 122402.
[45] J. Zehner, D. Wolf, M. U. Hasan, M. Huang, D. Bono, K. Nielsch, K. Leistner, G. S. D. Beach, *Phys. Rev. Mater.* **2021**, *5*, L061401.
[46] C. J. Jensen, A. Quintana, M. Sall, L. H. Diez, J. Zhang, X. Zhang, D. Ravelosona, K. Liu, *J. Magn. Magn. Mater.* **2021**, *540*, 168479.
[47] P. D. Murray, C. J. Jensen, A. Quintana, J. Zhang, X. Zhang, A. J. Grutter, B. J. Kirby, K. Liu, *ACS Appl. Mater. Interfaces* **2021**, *13*, 38916.
[48] K. Leistner, J. Wunderwald, N. Lange, S. Oswald, M. Richter, H. Zhang, L. Schultz, S. Fähler, *Phys. Rev. B* **2013**, *87*, 224411.
[49] W. Hou, Z. Zhou, L. Zhang, S. Zhao, B. Peng, Z. Hu, W. Ren, Z. G. Ye, Z. De Jiang, M. Liu, *ACS Appl. Mater. Interfaces* **2019**, *11*, 21727.
[50] W. Hou, S. Zhao, T. Wang, M. Yao, W. Su, Z. Hu, Z. Zhou, M. Liu, *Appl. Surf. Sci.* **2021**, *563*, 150074.
[51] J. Walter, H. Wang, B. Luo, C. D. Frisbie, C. Leighton, *ACS Nano* **2016**, *10*, 7799.
[52] M. Weisheit, S. Fähler, A. Marty, Y. Souche, C. Poinsignon, D. Givord, *Science* **2007**, *315*, 349.
[53] H. Gleiter, J. Weissmüller, O. Wollersheim, R. Würschum, *Acta Mater.* **2001**, *49*, 737.
[54] J. De Rojas, J. Salguero, F. Ibrahim, M. Chshiev, A. Quintana, A. Lopeandia, M. O. Liedke, M. Butterling, E. Hirschmann, A. Wagner, L. Abad, J. L. Costa-Krämer, E. Menéndez, J. Sort, *ACS Appl. Mater. Interfaces* **2021**, *13*, 30826.
[55] P. Monalisha, Z. Ma, E. Pellicer, E. Menéndez, J. Sort, *Adv. Electron. Mater.* **2023**, *9*, 2300249.
[56] Z. Ma, P. Monalisha, Z. Tan, E. Pellicer, M. O. Liedke, M. Butterling, A. G. Attallah, E. Hirschmann, A. Wagner, F. Ibrahim, M. Chshiev, E. Menéndez, J. Sort, *J. Materiomics* **2023**, *7*, 2352.
[57] C. J. Jensen, A. Quintana, P. Quarterman, A. J. Grutter, P. P. Balakrishnan, H. Zhang, A. V. Davydov, X. Zhang, K. Liu, *ACS Nano* **2023**, *17*, 6745.
[58] J. De Rojas, J. Salguero, A. Quintana, A. Lopeandia, M. O. Liedke, M. Butterling, A. G. Attallah, E. Hirschman, A. Wagner, L. Abad, J. L. Costa-Krämer, J. Sort, E. Menéndez, *Phys. Rev. Appl.* **2021**, *16*, 034042.
[59] K. Suzuki, T. Kaneko, H. Yoshida, Y. Obi, H. Fujimori, H. Morita, *J. Alloys Compd.* **2000**, *306*, 66.
[60] M. Meinert, B. Büker, D. Graulich, M. Dunz, *Phys. Rev. B* **2015**, *92*, 144408.
[61] N. A. Gokcen, *Bull. Alloy Phase Diagrams* **1990**, *11*, 33.
[62] P. Zilske, D. Graulich, M. Dunz, M. Meinert, *Appl. Phys. Lett.* **2017**, *110*, 192402.
[63] M. Widenmeyer, L. Shlyk, N. Becker, R. Dronskowski, E. Meissner, R. Niewa, *Eur. J. Inorg. Chem.* **2016**, *2016*, 4792.
[64] M. B. Lourenço, M. D. Carvalho, P. Fonseca, T. Gasche, G. Evans, M. Godinho, M. M. Cruz, *J. Alloys Compd.* **2014**, *612*, 176.
[65] Y. Qian, Z. Liu, H. Zhang, P. Wu, C. Cai, *ACS Appl. Mater. Interfaces* **2016**, *8*, 32875.
[66] A. Jain, S. P. Ong, G. Hautier, W. Chen, W. D. Richards, S. Dacek, S. Cholia, D. Gunter, D. Skinner, G. Ceder, K. A. Persson, *APL Mater.* **2013**, *1*, 011002.
[67] J. Häglund, A. Fernández, G. Grimvall, M. Körling, *Phys. Rev. B* **1993**, *48*, 11685.
[68] J. Nogués, J. Sort, V. Langlais, V. Skumryev, S. Suriñach, J. S. Muñoz, M. D. Baró, *Phys. Rep.* **2005**, *422*, 65.
[69] M. J. Carey, A. E. Berkowitz, *Appl. Phys. Lett.* **1992**, *60*, 3060.
[70] A. J. Devasahayam, M. H. Kryder, *IEEE Trans. Magn.* **1995**, *31*, 3820.
[71] T. Ambrose, K. Liu, C. L. Chien, *J. Appl. Phys.* **1999**, *85*, 6124.
[72] M. Takano, T. Terashima, Y. Bando, H. Ikeda, *Appl. Phys. Lett.* **1987**, *51*, 205.
[73] M. Tabuchi, M. Takahashi, F. Kanamaru, *J. Alloys Compd.* **1994**, *210*, 143.
[74] Z. Chen, C. J. Jensen, C. Liu, X. Zhang, K. Liu, *Appl. Phys. Lett.* **2023**, *123*, 082403.
[75] M. Mekata, J. Haruna, H. Takaki, *J. Physical Soc. Japan* **1968**, *25*, 234.
[76] J. Nogués, I. K. Schuller, *J. Magn. Magn. Mater.* **1999**, *192*, 203.
[77] A. N. Dobrynin, D. N. Ievlev, K. Temst, P. Lievens, J. Margueritat, J. Gonzalo, C. N. Afonso, S. Q. Zhou, A. Vantomme, E. Piscopiello, G. Van Tendeloo, *Appl. Phys. Lett.* **2005**, *87*, 12501.
[78] R. Krause-Rehberg, H. S. Leipner, *Positron Annihilation in Semiconductors: Defect Studies*, Springer, Berlin **1999**.
[79] F. Tuomisto, I. Makkonen, *Rev. Mod. Phys.* **2013**, *85*, 1583.
[80] K. Wada, T. Hyodo, *J. Phys. Conf. Ser.* **2013**, *443*, 012003.
[81] Y. Liu, J. Zhang, Y. Li, Q. Qian, Z. Li, Y. Zhu, G. Zhang, *Nat. Commun.* **2020**, *11*, 1853.
[82] Y. Fang, Y. Xue, Y. Li, H. Yu, L. Hui, Y. Liu, C. Xing, C. Zhang, D. Zhang, Z. Wang, X. Chen, Y. Gao, B. Huang, Y. Li, *Angew. Chem., Int. Ed.* **2020**, *59*, 13021.
[83] K. Ito, Y. Yasutomi, S. Zhu, M. Nurmamat, M. Tahara, K. Toko, R. Akiyama, Y. Takeda, Y. Saitoh, T. Oguchi, A. Kimura, T. Suemasu, *Phys. Rev. B* **2020**, *101*, 104401.
[84] H. Jung, S. J. Lee, M. Song, S. Lee, H. J. Lee, D. H. Kim, J. S. Kang, C. L. Zhang, S. W. Cheong, *New J. Phys.* **2009**, *11*, 043008.
[85] T. Komori, T. Horiuchi, H. Mitarai, T. Yasuda, K. Amemiya, T. Suemasu, *J. Magn. Magn. Mater.* **2022**, *564*, 170050.
[86] K. Ito, S. Honda, T. Suemasu, *Nanotechnology* **2022**, *33*, 062001.
[87] J. Stöhr, *J. Electron. Spectrosc.* **1995**, *75*, 253.
[88] C. Piamonteze, P. Miedema, F. M. F. De Groot, *Phys. Rev. B* **2009**, *80*, 184410.
[89] A. Barla, J. Nicolás, D. Cocco, S. M. Valvidares, J. Herrero-Martín, P. Gargiani, J. Moldes, C. Ruget, E. Pellegrin, S. Ferrer, *J. Synchrotron Radiat.* **2016**, *23*, 1507.
[90] A. Wagner, M. Butterling, M. O. Liedke, K. Potzger, R. Krause-Rehberg, *AIP Conf. Proc.* **2018**, *1970*, 40003.
[91] E. Hirschmann, M. Butterling, U. Hernandez Acosta, M. O. Liedke, A. G. Attallah, P. Petring, M. Görler, R. Krause-Rehberg, A. Wagner, *J. Instrum.* **2021**, *16*, P08001.
[92] J. V. Olsen, P. Kirkegaard, N. J. Pedersen, M. Eldrup, *Phys. Status Solidi C* **2007**, *4*, 4004.
[93] M. O. Liedke, W. Anwand, R. Bali, S. Cornelius, M. Butterling, T. T. Trinh, A. Wagner, S. Salamon, D. Walecki, A. Smekhova, H. Wende, K. Potzger, *J. Appl. Phys.* **2015**, *117*, 163908.
[94] M. J. Puska, R. M. Nieminen, *J. Phys. F Met. Phys.* **1983**, *13*, 333.
[95] E. Boroński, R. M. Nieminen, *Phys. Rev. B* **1986**, *34*, 3820.